

An engineered biosensor enables dynamic aspartate measurements in living cells

Kristian Davidsen^{1,2}, Jonathan S Marvin^{3*}, Abhi Aggarwal³, Timothy A Brown³, Lucas B Sullivan^{1*}

*For correspondence:

marvinj@janelia.hhmi.org (JSM);
lucas@fredhutch.org (LBS)

¹Human Biology Division, Fred Hutchinson Cancer Center, Seattle, WA, USA; ²Molecular and cellular biology program, University of Washington, Seattle, WA, USA; ³Howard Hughes Medical Institute (HHMI), Janelia Research Campus, Ashburn, VA, USA

Abstract Intracellular levels of the amino acid aspartate are responsive to changes in metabolism in mammalian cells and can correspondingly alter cell function, highlighting the need for robust tools to measure aspartate abundance. However, comprehensive understanding of aspartate metabolism has been limited by the throughput, cost, and static nature of the mass spectrometry based measurements that are typically employed to measure aspartate levels. To address these issues, we have developed a GFP-based sensor of aspartate (jAspSnFR3), where the fluorescence intensity corresponds to aspartate concentration. As a purified protein, the sensor has a 20-fold increase in fluorescence upon aspartate saturation, with dose dependent fluorescence changes covering a physiologically relevant aspartate concentration range and no significant off target binding. Expressed in mammalian cell lines, sensor intensity correlated with aspartate levels measured by mass spectrometry and could resolve temporal changes in intracellular aspartate from genetic, pharmacological, and nutritional manipulations. These data demonstrate the utility of jAspSnFR3 and highlight the opportunities it provides for temporally resolved and high throughput applications of variables that affect aspartate levels.

Introduction

The primary tool used by metabolism researchers, mass spectrometry (MS) coupled with either gas chromatography (GCMS) or liquid chromatography (LCMS), involves extracting pools of thousands of cells and measuring the liberated metabolites. This approach is powerful but has significant drawbacks; it requires highly specialized equipment, it is expensive, and sample preparation by chemical extractions homogenizes metabolic differences that may occur amongst different cells in complex samples or across subcellular compartments. Metabolite extraction also consumes precious samples that might otherwise be desirable to analyze over time or with additional outputs. Development of genetically encoded protein sensors (biosensors) over the past two decades has provided new opportunities to visualize the release, production, and depletion of important signaling molecules and metabolites with subsecond and subcellular resolution (reviewed in [Kostyuk et al. \(2019\)](#); [Koveal et al. \(2020\)](#)). Thus, with the trade-off of only monitoring one metabolite per sensor, biosensors provide a solution to many of the problems inherent to metabolite extraction and MS.

Aspartate is amongst the most concentrated metabolites in cells ([Park et al., 2016](#)), yet it is one of only two amino acids that is not predominantly acquired from the environment. While the

41 other, glutamate, is made from glutamine by the enzyme glutaminase, no analogous enzyme exists
42 in humans to convert asparagine to aspartate (*Sullivan et al., 2018*). Instead, aspartate must be
43 synthesized by transamination of the tricarboxylic acid (TCA) cycle metabolite oxaloacetate by the
44 cytosolic enzyme GOT1 or the mitochondrial enzyme GOT2. Notably, aspartate synthesis can oc-
45 cur from multiple metabolic sources *via* complex metabolic reactions occurring in both the cytosol
46 and mitochondria, rendering aspartate levels at the whole cell and subcellular levels dependent
47 on multiple metabolic variables. For example, impairments to mitochondrial respiration can de-
48 plete aspartate levels and aspartate restoration can reestablish proliferation in cells with defective
49 mitochondria (*Sullivan et al., 2015; Birsoy et al., 2015; Cardaci et al., 2015; Hart et al., 2023*). Alter-
50 ations to aspartate levels are associated with modifications to cell function in multiple biological
51 processes, including stem cells (*Tournaire et al., 2022; Arnold et al., 2022*), immune cells (*Bailis*
52 *et al., 2019*), endothelial cells (*Diebold et al., 2019*), and cancer (*Helenius et al., 2021*). In addition,
53 genetic methods to elevate intracellular aspartate can impact biology *in vivo*, increasing tumor
54 growth (*Sullivan et al., 2018; Garcia-Bermudez et al., 2018*) and improving hematopoietic function
55 (*Qi et al., 2021*). Therefore, our understanding of metabolism in multiple biological systems could
56 be improved with the availability of an aspartate biosensor.

57 We have previously developed a biosensor for glutamate (iGluSnFR) using the *E.coli* glutamate/aspartate
58 binding domain (Gltl) linked to circularly permuted GFP (*Marvin et al., 2013*), and subsequently
59 optimized it by modulating its affinity, kinetics, color, and total fluorescence change (SF-iGluSnFR
60 and iGluSnFR3) (*Marvin et al., 2018; Aggarwal et al., 2023*). Since the Gltl domain also binds aspar-
61 ate, albeit at lower affinity than glutamate (*Hu et al., 2008*), we reasoned that subtle modifications
62 to the ligand binding site could switch the relative aspartate/glutamate specificity. We achieved this
63 using a small mutagenesis screen on a precursor to iGluSnFR3 (Supplementary file 1), guided by
64 the crystal structure of glutamate-bound Gltl. The resulting biosensor, jAspSnFR3, was character-
65 ized *in vitro* and in cells with matched LCMS determined aspartate levels, showing that it accurately
66 reports genetic, pharmacological, and nutritional manipulation of intracellular aspartate.

67 Results

68 Protein engineering

69 We observed that the glutamate sensor, iGluSnFR, binds both glutamate and aspartate, with higher
70 affinity for the former (*Marvin et al., 2013*). To shift the relative affinities of the two ligands, we
71 evaluated the structure of the binding pocket (*Hu et al., 2008*), and sampled all possible amino acid
72 substitutions of residue S72, which interacts with the side-chain carboxylate of bound glutamate
73 (*Figure 1*, panel A). By expressing mutant sensors in bacteria and measuring the fluorescence of
74 bacterial lysate in response to aspartate and glutamate, we identified S72A and S72P as having
75 switched specificity from glutamate to aspartate. S72T, identified in a faster version of iGluSnFR
76 (*Helassa et al., 2018*), also preferentially binds aspartate over glutamate.

77 As an improved glutamate sensor (iGluSnFR3) was being developed (*Aggarwal et al., 2023*),
78 we took a variant from that process and queried the effect of S72A, S72T, and S72P on aspar-
79 ate/glutamate affinity. In bacterial cell lysate, S72P maintained the expected shift to a preference
80 for aspartate when inserted into a iGluSnFR3 precursor, and had a higher fluorescence fold in-
81 crease ($\Delta F/F$) than either S72A or S72T (*Figure 1—figure Supplement 1*, panel A). To further increase
82 specificity of the S72P mutant, we sampled mutations at S27, which also interacts with the carboxy-
83 late of bound glutamate. One of those, S27A, had lower affinity for glutamate while mostly main-
84 taining affinity for aspartate (*Figure 1—figure Supplement 1*, panel A). We then moved forward
85 with this variant, and since it is built from a precursor of iGluSnFR3, named it Janelia-developed
86 Aspartate-Sensing Fluorescent Reporter (jAspSnFR3). Since we expected to be using this sensor
87 in cell culture studies, and potentially *in vivo*, over the course of hours or even days, we added a
88 C-terminal red fluorescence protein, mRuby3, to enable correction for expression. All biochemical
89 characterization is reported with jAspSnFR3-mRuby3. For jAspSnFR3 signal normalization in cells

90 we used a mix of jAspSnFR3-mRuby3 and nuclear localized mRuby2.

91 Further characterization of the sensor found it is yellow-shifted in excitation and emission compared to typical GFP-based sensors, since its chromophore is formed by the triad of GYG and has 92 the T203Y pi-stacking mutations of the Venus yellow fluorescent protein. This yellow-shift facilitates 93 observation deeper into tissues using 2-photon microscopy, as the sensor has high signal fold 94 change and significant 2-photon cross-section at 1040 nm (*Figure 1—figure Supplement 1*, 95 panel B). It has a K_D for aspartate of about 50 μM and binds glutamate and asparagine with K_D 96 greater than 5 mM (*Figure 1*, panel B). The sensor also does not appreciably change its green fluorescence 97 in response to other amino acids (*Figure 1—figure Supplement 2*, panel A) or to other decoys 98 considered relevant to aspartate metabolism, including pharmacological treatments (*Figure 99 1—figure Supplement 2*, panel B). We performed rapid-mixing stopped-flow fluorescence spectroscopy 100 to determine the aspartate binding kinetics and measured an on-rate of 0.8 $\mu\text{M}^{-1} \text{ sec}^{-1}$ 101 and an off-rate of 26 sec $^{-1}$, resulting in a K_D of 33 μM in agreement with equilibrium measurements 102 (*Figure 1—figure Supplement 3*). The off-rate corresponds to a time to equilibrium of 130 msec. when defined using five half-lives (*Jarmoskaite et al., 2020*).

103 Surprisingly, the mRuby3 fluorescence of affinity-purified jAspSnFR3.mRuby3 responds to some 104 amino acids at high millimolar concentrations, indicating a non-specific effect (*Figure 1—figure 105 Supplement 4*, panel A). This was determined to be due to an unexpected interaction with the 106 C-terminal histidine tag and could be reproduced with other proteins containing mRuby3 and purified 107 via the same C-terminal histidine tag (*Figure 1—figure Supplement 4*, panel B and C). Interestingly, 108 a structurally related, non-amino acid compound, GABA, does not elicit a change in red fluorescence; 109 indicating, that only amino acids are interacting with the histidine tag (*Figure 1—figure 110 Supplement 4*, panel D). Nevertheless, most of our cell culture experiments were performed 111 with nuclear localized mRuby2, which lacks a C-terminal histidine tag, and these measurements 112 correlated with those using the histidine tagged jAspSnFR3-mRuby3 construct (*Figure 1—figure 113 Supplement 1*, panel D).

114 A recently described and concurrently developed biosensor for aspartate is reported to be 115 adversely affected by temperatures higher than 30°C, causing lower maximum $\Delta F/F$ (*Hellweg et al., 116 2023*). Our aspartate sensor appears unaffected by temperature up to 37°C, with the same maximum 117 $\Delta F/F$ at 37°C as compared to 30°C (*Figure 1—figure Supplement 2*, panel C). Like all cpGFP- 118 based sensors, it is sensitive to pH but changes in fluorescence due to aspartate far exceed what 119 one might expect from changes in fluorescence due to physiologically attainable changes in intra- 120 cellular pH (*Figure 1—figure Supplement 2*, panel D). To determine whether it had the potential to 121 serve as an aspartate biosensor in mammalian cells, we expressed jAspSnFR3 in H1299 cells along 122 with nuclear-RFP. Expression of jAspSnFR3 had no obvious toxic effects and H1299 jAspSnFR3 cells 123 had visible fluorescence in the green channel (*Figure 1*, panel C). As it is the primary substrate for 124 aspartate production, glutamine removal is expected to deplete aspartate levels. Indeed, we found 125 that 24 hours of glutamine withdrawal abolished GFP signal while leaving RFP unchanged. These 126 findings therefore supported the further testing of jAspSnFR3 as a method to quantify aspartate 127 levels over time in live mammalian cells.

128 **jAspSnFR3 reveals the temporal dynamics of aspartate limitation**

129 Having shown that jAspSnFR3-mRuby3 protein can measure the concentration of aspartate *in vitro*, 130 we wanted to test the usefulness of the sensor in cells. To that end, we generated stable cell lines 131 with constitutive expression of jAspSnFR3-mRuby3 or jAspSnFR3 and nuclear localized RFP, and 132 generated single cell clones from each to yield cell lines with uniform expression. In each case, 133 we then normalized GFP sensor signal to RFP signal to control for expression differences within 134 and across cell lines. We also noted that normalization with nuclear RFP and RFP fusion were 135 highly correlated, enabling jAspSnFR3 sensor applications where nuclear RFP labeling is desirable 136 e.g. for counting cells at multiple timepoints using live cell imaging (*Figure 2—figure Supplement 1*, 137 panel D). An important motivation for using a biosensor for tracking aspartate changes is to enable 138

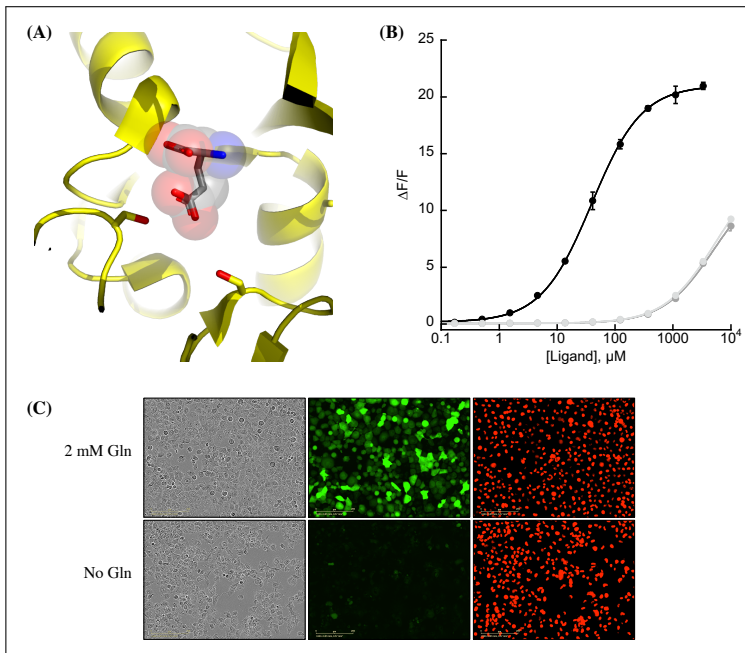


Figure 1. Protein engineering and *in vitro* characterization. (A) Structure of the binding pocket of glutamate-bound Gtl1 (2VHA.pdb) with residues S72 (left) and S27 (right) shown as sticks and bound glutamate as sticks inside transparent spheres. (B) Fluorescence response of purified jAspSnFR3-mRuby3 when titrated with aspartate (black) or glutamate or asparagine (grey tones). Ex. 485 nm (20 nm bandpass), Em. 535 nm (20 nm bandpass). Error bars are s.d. of three technical replicates. (C) Live cell imaging in the phase contrast, GFP and RFP channels of H1299 Nuclear-RFP cells expressing jAspSnFR3 after 24 hours with/without glutamine.

Figure 1—figure supplement 1. Aspartate specificity and excitation/emission spectra.

Figure 1—figure supplement 2. Decoy, temperature and pH sensitivity.

Figure 1—figure supplement 3. Stopped-flow kinetics.

Figure 1—figure supplement 4. mRuby3 interaction with histidine tag.

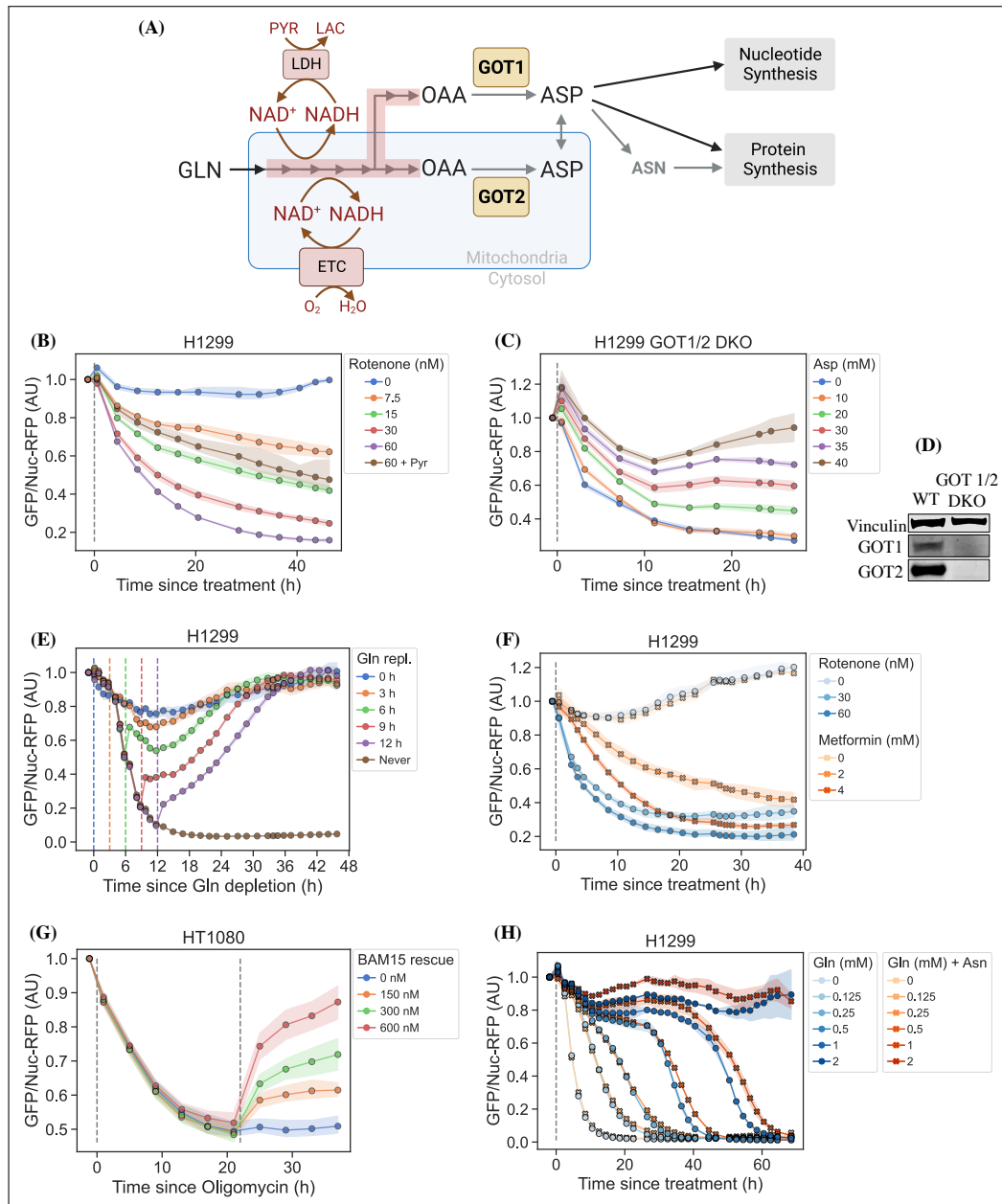
140 temporal measurements on the same subset of live cells, therefore we used an Incucyte S3 which
141 performs live cell imaging under native cell line growth conditions.

142 Cellular aspartate levels depend on the availability of metabolic precursors and the activity
143 of several metabolic processes. One such process is the generation of a sufficiently large intra-
144 cellular NAD+/NADH ratio to drive aspartate precursor synthesis, a process normally maintained
145 through mitochondrial respiration or, in its absence, by treatment with exogenous electron ac-
146 ceptors like pyruvate (*Figure 2*, panel A). Genetic alterations and pharmacological treatments that
147 disrupt mitochondrial respiration can decrease NAD+/NADH and aspartate levels, both of which
148 can be partially restored by supplementation with pyruvate (*Sullivan et al., 2015; Birsoy et al.,*
149 *2015*). We thus tested the ability of jAspSnFR3 to quantify depletion of intracellular aspartate abun-
150 dance upon treatment with the mitochondrial complex I inhibitor rotenone and the partial rescue
151 of aspartate by supplementing cells with pyruvate. Titrating rotenone in H1299 cells, we observed
152 a dose dependent decrease in sensor fluorescence with increased rotenone, corresponding to
153 the expected decrease in aspartate synthesis capacity, and a partial restoration of fluorescence in
154 cells co-treated with pyruvate (*Figure 2*, panel B). This observation was extended to different cell
155 lines with different rotenone sensitivities, corroborating the observation of decreased sensor flu-
156 orescence upon rotenone treatment and rescue by pyruvate supplementation (*Figure 2—figure*
157 *Supplement 1*, panel A, B and E). Furthermore, we tested and confirmed the ability of pyruvate
158 to rescue aspartate levels after an initial depletion phase with rotenone, thus confirming that the
159 sensor is also able to measure the reverse kinetics of aspartate restoration (*Figure 2—figure Sup-*
160 *plement 1*, panel C).

161 We next evaluated the ability of the sensor to measure changes in aspartate without requiring
162 treatment with a mitochondrial inhibitor. To this aim, we used CRISPR/Cas9 to generate an H1299
163 cell line with a double knockout (DKO) of the genes glutamic oxalacetic transaminases 1 and 2
164 (GOT1/2 DKO), which renders cells unable to synthesize aspartate and therefore dependent on
165 aspartate uptake from the media (Garcia-Bermudez *et al.*, 2022). Using these H1299 GOT1/2 DKO
166 cells, we titrated media aspartate and observed that sensor fluorescence decreased upon aspar-
167 tate withdrawal, approaching a steady-state after approximately 11 hours, that corresponded to
168 the aspartate availability in the media (Figure 2, panel C). We note that 10 mM media aspartate, a
169 higher concentration than any other amino acid in media, is still unable to rescue sensor signal sig-
170 nificantly above aspartate depleted media. This confirm previous observations that aspartate has
171 poor cell permeability and often requires concentrations of 20 mM or more to robustly contribute
172 to intracellular aspartate pools (Sullivan *et al.*, 2018).

173 Finally, we evaluated the ability of the sensor to measure rapid decreases/increases in aspartate
174 levels. In most cancer cell lines, intracellular aspartate is derived primarily from glutamine oxida-
175 tion, thus making glutamine depletion and restoration an entry point for affecting aspartate levels.
176 Glutamine withdrawal from H1299 cells showed a rapid depletion in sensor fluorescence with a
177 low level steady-state reached after approximately 12-16 h (Figure 2, panel E). In the same cells,
178 glutamine repletion, after different times of glutamine depletion, caused an initial rapid increase
179 in sensor fluorescence followed by a slower adjustment phase before reaching baseline. Particu-
180 larly interesting is the sensor readings for cells repleted with glutamine 6 h after withdrawal, show-
181 ing a rapid increase followed by a decrease, before a slow increase to baseline. We concurrently
182 measured the cell count over time by counting RFP fluorescent nuclei and the cell confluence (Fig-
183 ure 2—figure Supplement 2, panel A and B). These data confirm that cells remain viable 12 h after
184 glutamine withdrawal and that proliferation rates are first fully recovered when aspartate levels
185 reach baseline. Interestingly, the proliferation rate undergoes a similar multi-phase recovery as the
186 aspartate sensor signal. We suspect these phases to be driven by low aspartate causing S-phase
187 arrest during glutamine deprivation (Patel *et al.*, 2016), and although more evidence is necessary
188 to prove this suspicion, our data show that an aspartate sensor is an excellent tool towards this
189 end.

190 Metformin has slower inhibitor kinetics compared to rotenone
191 Metformin is a commonly used diabetes treatment that has been shown to act as a mitochon-
192 drial complex I inhibitor (Owen *et al.*, 2000; El-Mir *et al.*, 2000; Andrzejewski *et al.*, 2014; Wheaton
193 *et al.*, 2014) and can decrease intracellular aspartate levels in a dose responsive way (Gui *et al.*,
194 2016). Whereas rotenone is a lipophilic molecule that can cross the cell membrane and act rapidly,
195 metformin is hydrophilic and poorly permeable to most cells, resulting in comparatively delayed
196 kinetics for metformin to decrease mitochondrial respiration in intact cells. As rotenone and met-
197 formin are often used interchangeably as complex I inhibitors, we wondered whether they have
198 an equivalent temporal effect on aspartate or if the delayed effects of metformin on mitochondrial
199 inhibition would similarly delay its effects on aspartate levels. To test this, we treated cells with two
200 doses each of rotenone and metformin with roughly equivalent aspartate lowering effects and fol-
201 lowed the sensor signal over time (Figure 2, panel F). We observed that the aspartate depleting
202 effects of metformin acted slower than rotenone, with 30 nM rotenone reaching steady-state after
203 ~20 hours and 2 mM metformin reaching a similar sensor response after almost 40 hours. These
204 data therefore provide orthogonal confirmation of the differential kinetics of these drugs on cell
205 metabolism and highlight the temporal opportunities enabled by measuring aspartate levels by
206 jAspSnFR3.



207 Oligomycin induced decrease in aspartate can be rescued by uncoupling the mitochondrial membrane potential
 208
 209 Oligomycin A binds to and inhibits the proton coupled rotation of ATP synthase (Symersky *et al.*,
 210 2012). This inhibition leads to a slowing of the electron transfer in the mitochondrial electron trans-
 211 port chain by hyperpolarizing the membrane potential (Brand and Nicholls, 2011) and it has pre-
 212 viously been shown that the cellular effects of oligomycin can be rescued by partial uncoupling of
 213 the mitochondrial membrane potential (Sullivan *et al.*, 2015; To *et al.*, 2019). We used our aspar-
 214 tate sensor to show that oligomycin induces a decrease in aspartate and that the mitochondrial
 215 membrane potential specific uncoupler BAM15 (Kenwood *et al.*, 2014) can partially restore this
 216 aspartate level (Figure 2, panel G), thus confirming previous observations and illustrating the ver-
 217 satility of the our sensor.

Figure 2. jAspSnFR3 resolves temporal aspartate changes in live cells. (A) Overview of aspartate metabolism, highlighting how glutamine depletion, mitochondrial inhibition, GOT1/2 knockout and pyruvate/asparagine supplementation can impact aspartate levels. (B) H1299 cells treated with a rotenone titration and rescued by co-treatment with pyruvate. (C) H1299 GOT1/2 double knockout cells grown in media with 40 mM aspartate, washed thrice in media without aspartate and then changed into media with a titration of aspartate. (D) Western blot verification of H1299 GOT1/2 double knockout. (E) H1299 cells changed into media without glutamine and then glutamine repleted (repl.) at the different timepoints. (F) H1299 cells treated with either rotenone or metformin to compare inhibitor kinetics. (G) HT1080 cells treated with oligomycin A and after 22 h rescued with a titration of mitochondrial uncoupler BAM15. (H) H1299 cells changed into media with a titration of glutamine with or without 1 mM asparagine. For (B), (C), (E), (F), (G) and (H) sensor signal over time shown as RFP normalized jAspSnFR3 signal following various perturbations of live cells. All experiments shown are normalized to a pre-treatment scan and then treated with the specified drug or amino acid. Grey dashed lines indicate the time of treatment. Colored dashed lines indicate the time of treatment for multiple treatments in the same plot. Markers indicate the average using available well replicates and are superimposed on a bootstrapped 95% confidence interval colored using the same color code as the markers. GLN, glutamine. ETC, electron transport chain. LDH, lactate dehydrogenase. OAA, oxaloacetic acid. ASP, aspartate. ASN, asparagine. AU, arbitrary unit.

Figure 2—figure supplement 1. Rotenone titration in different cell lines.

Figure 2—figure supplement 2. Plots related to glutamine limitation.

218 Asparagine salvage diverts glutamine consumption

219 It has previously been reported that asparagine, a product of aspartate metabolism, becomes es-
220 sential upon glutamine starvation (*Pavlova et al., 2018; Zhang et al., 2014*). We hypothesize that
221 asparagine becomes essential in these conditions because glutamine starvation decreases synthe-
222 sis of aspartate, slowing asparagine production, and because asparagine supplementation spares
223 aspartate consumption, allowing it to be redirected into other essential fates. However, it has been
224 difficult to measure metabolic changes during glutamine limitation because continuous glutamine
225 consumption during the course of the experiment will result in progressive glutamine depletion
226 and further developing metabolic effects. One solution to this problem is to measure the temporal
227 changes in aspartate levels over the course of glutamine starvation and, indeed, we found that full
228 glutamine depletion has a rapid and drastic effect on sensor signal (**Figure 2**, panels E and H and **Fig-**
229 *ure 2—figure Supplement 2*, panel C). Interestingly, aspartate signal did not robustly correlate with
230 the concentration of glutamine in the media in the short term, but instead we found that higher
231 amounts of glutamine in the media delayed the time until aspartate depletion, presumably corre-
232 sponding to the time at which glutamine is fully depleted and unable to support further aspartate
233 synthesis. Furthermore, we found that adding 1 mM asparagine delayed the decrease in sensor
234 signal, suggesting that when asparagine can be salvaged from the media it diverts glutamine con-
235 sumption that would otherwise be purposed for asparagine synthesis via aspartate consumption.
236 We note that, as this data is produced in real-time, the method can be used to dynamically find the
237 optimal sampling times to measure and compare intracellular levels of other metabolites relevant
238 to glutamine starvation using mass spectrometry.

239 jAspSnFR3 signal correlates with intracellular aspartate concentration

240 It is an important requirement for an aspartate sensor that it reflects the intracellular concentra-
241 tion of aspartate over a biologically relevant range for several cell lines. Reference points for the
242 intracellular aspartate concentration can be generated using metabolite extraction and LCMS, but
243 it is important to note that this technique reports the total amount of aspartate summed across all
244 compartments, which can differ in their aspartate concentration (*Chen et al., 2016*). The LCMS de-
245 rived concentration also does not reflect protein crowding, aspartate binding to enzymes, or other
246 factors that would affect the free aspartate concentration. Nevertheless, LCMS is the standard ap-
247 proach in studying metabolism and has previously been used to correlate aspartate levels with cell
248 proliferation (*Gui et al., 2016; Hart et al., 2023*). Thus, we titrated mitochondrial inhibitors of com-
249 plex I (rotenone and metformin) and complex III (antimycin A), with or without pyruvate rescue, in

250 three different cell lines and waited 24 hours until aspartate had reached near steady-state levels
251 before conducting a final measurement of sensor fluorescence, followed by immediate metabo-
252 lite extraction and quantitative LCMS measurements of aspartate levels using isotope dilution. We
253 then compared sensor signals to LCMS derived aspartate concentrations and fitted a Hill curve
254 to infer the intracellular aspartate concentrations at half-maximum sensor signal (**Figure 3**). For
255 all three cell lines, we observe a monotonically increasing relationship between sensor signal and
256 intracellular aspartate concentration, covering around two orders of magnitude. We also observe
257 no relationship between sensor signal and intracellular glutamate levels (**Figure 3—figure Supple-**
258 **ment 1**). These observations validate the utility of our sensor in a biologically relevant range of
259 aspartate concentrations without interference from glutamate.

260 Interestingly, the intracellular aspartate concentrations at half-maximum sensor fluorescence
261 is more than 17 fold higher than the aspartate K_D determined by *in vitro* characterization of the
262 sensor. While the numbers inferred for intracellular aspartate are only point estimates, it is highly
263 unlikely that they are inaccurate to this degree. We speculate that the apparent cytosolic aspartate
264 concentration is likely lower than the total aspartate concentration summed across all compart-
265 ments. This suggests that binding of aspartate by jAspSnFR3 is in competition with other proteins
266 and highlights that another advantage of using a biosensor is that measurements are made relative
267 to their native environment.

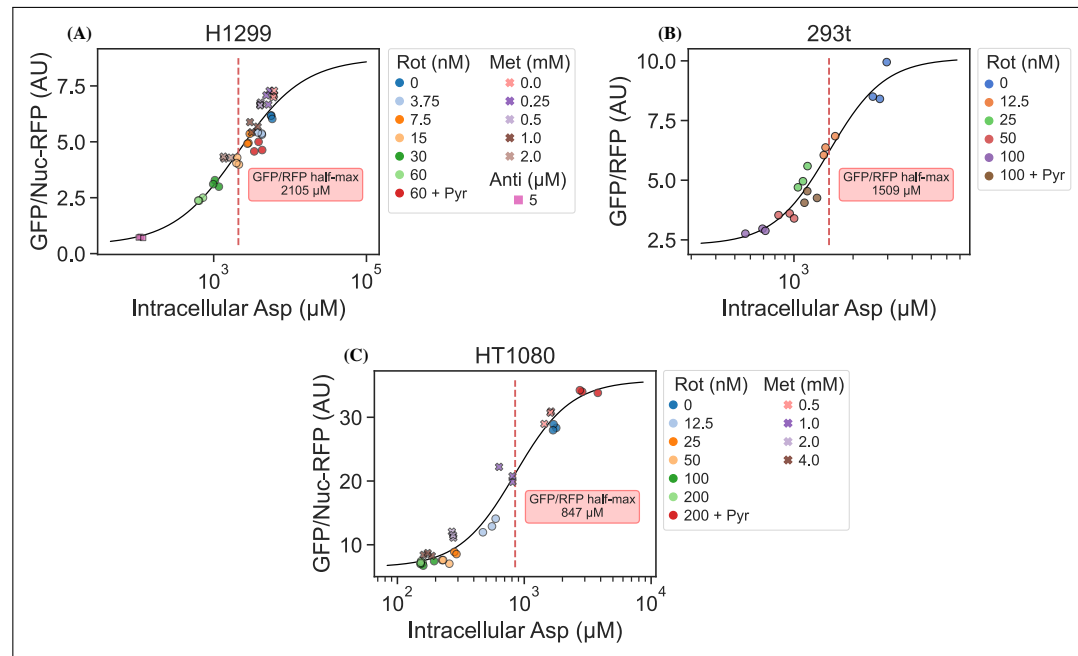


Figure 3. jAspSnFR3 signal predicts LCMS measured intracellular aspartate concentration. A Hill equation with top and bottom asymptotes, midpoint and slope as free variables is fitted to the datapoints and shown by the black line. The intracellular aspartate concentration at the inferred half maximum of RFP normalized jAspSnFR3 signal is reported in the red inserts. (A) Rotenone, metformin and antimycin A titrations in H1299 cells. (B) Rotenone titration in HEK293t cells. (C) Rotenone and metformin titrations in HT1080 cells. Markers indicate a single well from which both LCMS and jAspSnFR3 data was collected. Replicate wells have identical color and marker shape. AU, arbitrary unit.

Figure 3—figure supplement 1. jAspSnFR3 signal does not correlate with glutamate concentration.

268 Discussion

269 A biosensor for aspartate is an important step towards improved understanding of aspartate metabolism.
270 We have shown that our jAspSnFR3 sensor can resolve temporal changes in intracellular aspartate
271 to answer questions that would be impractical using LCMS. In most studies involving aspartate

272 metabolism, metabolite extraction is performed 6-16 hours after treatment with the implicit as-
273 sumption that this is enough time to reach metabolic steady-state. Using our sensor, we have
274 shown that the time to reach steady-state can be much longer and depends on the treatment. Fu-
275 ture studies seeking to understand the effects of treatments affecting aspartate levels can there-
276 fore use real-time measurements using jAspSnFR3 to determine when cells have reached steady-
277 state and then perform metabolite extraction for LCMS.

278 Recently, a concurrently developed aspartate sensor based on SF-iGluSnFR was reported by
279 another group (*Hellweg et al., 2023*). That aspartate sensor started with the S72A mutation, but
280 then included 6 additional mutations identified by a combination of targeted screening and deep
281 mutational scanning. Our design differs from the one by *Hellweg et al. (2023)* by 25 mutations
282 (Supplementary file 1). Notably, we achieved aspartate selectivity by generating only two muta-
283 tions in the binding pocket of its precursor, and so the majority of these amino acid differences
284 derive from us building off the next generation precursor for iGluSnFR3, which has increased $\Delta F/F$
285 compared to iGluSnFR. Indeed, the sensor described here appears to have a larger signal change
286 both *in vitro* and in live cells, although head-to-head comparisons have not been performed. Im-
287 portantly, while the sensor from *Hellweg et al. (2023)* is adversely affected by temperature at 37°C,
288 our sensor is not, allowing us to perform cell culture experiments at standard incubation condi-
289 tions. Another difference is that our jAspSnFR3 sensor has a higher affinity for all three relevant lig-
290 ands (aspartate, asparagine, and glutamate); however, we found no discernible effect of treatment
291 with 1 mM asparagine on sensor signal in cell culture experiments and found no correlation be-
292 tween intracellular glutamate concentration and sensor fluorescence across treatment conditions
293 (*Figure 3—figure Supplement 1*). Collectively, we conclude that the jAspSnFR3 aspartate sensor
294 reported here has biochemical features that makes it ideal for measuring intracellular aspartate
295 levels in live cells.

296 In summary, we report a novel fluorescence based biosensor that enables dynamic measure-
297 ments of aspartate. This tool is free of significant interference from relevant metabolites in phys-
298 iological intracellular systems and can resolve changes in aspartate from diverse treatment con-
299 ditions in live cells over time. This approach to measuring aspartate will also have advantages
300 compared to LCMS based metabolomics, including enabling high throughput experiments to iden-
301 tify variables that affect aspartate levels, such as testing the effects of a drug library on cells in
302 multiwell plates or using FACS based selection during genetic screens. Another potential use for
303 this sensor would be to dissect compartmentalized metabolism, with mitochondria being a criti-
304 cal target, although incorporating the influence of pH on sensor fluorescence will be an important
305 consideration in this context. Altogether, adoption of jAspSnFR3 to measure aspartate levels will
306 therefore provide novel opportunities to understand this critical node of cell metabolism.

307 Methods and Materials

308 Sensor engineering and screening

309 The starting template for jAspSnFR3 was a variant along the path of making iGluSnFR3 (sequence
310 information in Supplementary file 1). Site saturation mutagenesis at positions S72 and S27 was
311 achieved by the uracil template method (*Kunkel, 1985*). Mutant libraries (maximum theoretical di-
312 versity of 20 each) were transformed into T7 express cells. Individual colonies were picked into a
313 96-well plate containing auto-induction media (*Studier, 2005*) and shaken at 30°C for 18-24 hours,
314 then harvested by centrifugation. Cell pellets were resuspended in PBS and repelleted by centrifu-
315 gation 5 times over, then frozen as pellets overnight. The frozen 96-well plate was thawed by addi-
316 tion of room temperature PBS, agitated by vortexing to resuspend and lyse cells, and then pelleted
317 again. 100 μ L clarified lysate was added to each of two black 96-well plates and its fluorescence was
318 measured. Aspartate or glutamate was added (final concentration 100 μ M) and fluorescence was
319 measured again. Wells that had a higher $\Delta F/F$ for aspartate than glutamate were isolated, titrated
320 with aspartate and glutamate, and sequenced. After confirming that S72P was the most selective

321 variant for aspartate from a library of S72X, a library of S27X was made in the background of S72P.
322 The selection process was repeated, and S72P+S27A was identified as the "best" aspartate sensor
323 and named jAspSnFR3. mRuby3 was subsequently cloned at the C-terminus and this construct was
324 named jAspSnFR3-mRuby3.

325 **Protein expression and purification**

326 For large scale protein expression and purification, jAspSnFR3-mRuby3 was transformed into T7
327 express cells and a single colony was grown in 300 mL auto-induction media (*Studier, 2005*) at 30°C
328 for ~18 hours. Cells were pelleted by centrifugation at 6000g, resuspended in PBS and 1 M NaCl and
329 frozen. The resuspended cell pellet was thawed, sonicated on ice (5 sec on, 5 sec off, 10 min), and
330 centrifuged at 6000g to remove cellular debris. The lysate was further clarified by centrifugation
331 at 35,000g for 1 hour, and then purified by IMAC on a HisTrap FF column, with a 2 mL/min flow
332 rate and elution from 0 to 200 mM imidazole over 120 mL. Untagged mRuby2 and mRuby3 were
333 partially purified by DEAE anion exchange. Fluorescent fractions were pooled, concentrated by
334 ultrafiltration, and dialyzed in PBS to remove endogenously bound ligands. Protein concentration
335 was determined by alkaline denaturation, and measurement at A447 (Ext. Coeff. 44,000 M-1 cm-1).

336 **Sensor biochemical characterization**

337 *In vitro* fluorescence measurements were performed on a Tecan Spark plate reading fluorimeter at
338 ~28°C, with the exception of the controlled temperature measurement, in which a BioTek Cytaion
339 5 was used. Concentrated jAspSnFR3-mRuby3 protein was diluted to 0.2 μ M in PBS for all measure-
340 ments. Decoy amino acids and pharmacologues were purchased from Sigma-Aldrich and solvated
341 as 100 mM stocks in PBS, with the exception of rotenone, which was resuspended in DMSO. Titra-
342 tions were performed by making serial dilutions (1:2) of the stock compound into PBS, and adding
343 10 μ L of that to 100 μ L of 0.2 μ M protein solution. Fluorescence was measured before addition of
344 compound, and $\Delta F/F$ was calculated as $(F(\text{treatment}) - F(\text{initial})) / F(\text{initial})$.

345 Two-photon cross sections were collected for 1 μ M solutions of protein in PBS with or without 10
346 mM aspartate, excited by pulses from a mode-locked Ti:Sapphire laser (Chameleon Ultra, Coherent,
347 80 MHz, 140 fs pulse width, 1 mW power at the focus). Emission was detected by an avalanche
348 photodiode (PDM Series, Micro Photon Devices) with a 550 nm filter (88 nm bandpass).

349 Stopped-flow kinetics of binding were determined by mixing equal volumes of 0.2 μ M jAsp-
350 SnFR3 protein (in PBS, pH 7.4) with varying concentrations of aspartate in an Applied Photophysics
351 SX20 stopped flow fluorimeter with 490 nm LED excitation and 515 nm long pass filter at room tem-
352 perature (22°C). The increase in fluorescence upon mixing was observed with 1000 data points over
353 the course of 1 sec (1 msec per data point) and equilibrium was reached within 100 msec. Each mix-
354 ing was repeated five times and averaged. Standard deviations are excluded from the plots as the
355 error bars are nearly the same size as the data markers. The first 3 observations were discarded
356 to remove mixing artefacts and account for the dead time of the instrument. Data were plotted
357 and time courses were fit to a single rising exponential ($y - \text{intercept} + \text{total rise} * (1 - \exp(-k_{obs} * t))$)
358 using Kaleidagraph (version 5.01). To determine the kinetic rates, k_{obs} was plotted as a function of
359 aspartate concentration and the linear portion of that graph was fitted. The slope, corresponding
360 to the on-rate k_1 , was found to be 0.8 μ M-1 sec-1 and the y-intercept, corresponding to the off-rate
361 k_{-1} , was found to be 26 sec-1, resulting in a K_D of 33 μ M.

362 **Cell culture**

363 Cell lines were acquired from ATCC (HEK293T, H1299, HT1080) and tested to be free from my-
364 coplasma (Mycoprobe, R&D Systems). Cells were maintained in Dulbecco's Modified Eagle's Medium
365 (DMEM) (Gibco, 50-003-PB) supplemented with 3.7 g/L sodium bicarbonate (Sigma-Aldrich, S6297),
366 10% fetal bovine serum (FBS) (Gibco, 26140079) and 1% penicillin-streptomycin solution (Sigma-
367 Aldrich, P4333). Cells were incubated in a humidified incubator at 37°C with 5% CO2.

368 Generation of nuclear RFP cell lines

369 Nuclear RFP cell lines were generated using 1e5 transducing units of EF1A-nuclear RFP lentivirus
370 (Cellomics Technology, PLV-10205-50) by spinfection. Cells were seeded at 50% confluence in 6
371 well dishes, lentivirus was added to fresh media with 8 μ g/ μ L polybrene, then added to cells and
372 followed by centrifugation (900g, 90 mins, 30°C). Two days after infection, cells were sorted for high
373 RFP expression using fluorescence-activated cell sorting (FACS). High RFP cells were then expanded
374 and single-cell cloned by limiting dilution, plating 0.5 cells/well on a 96 well plate. Plates were then
375 screened for RFP expression and localization using Incucyte S3 (Sartorius) and a suitable clone
376 chosen, expanded, and used for all subsequent experiments.

377 Lentiviral production and stable cell line generation

378 jAspSnFR3 and jAspSnFR3-mRuby3 were first cloned into entry vector pENTR1A (Fisher, A10462)
379 using NEBuilder HiFi DNA Assembly Cloning Kit (New England BioLabs, E2621). These donor con-
380 structs were then used to transfer their insert into destination vectors: pLX304-CMV-Blast (Ad-
381 dgene, 25890), pLenti-CMV-Hygro (w117-1) (Addgene, 17454 a gift from Eric Campeau & Paul Kauf-
382 man), or pLX304-CAG-Blast using LR Clonase II (Fisher, 11791100). pLX304-CAG-Blast was gener-
383 ated in house by swapping the CMV promoter region of pLX304-CMV-Blast with a CAG promoter
384 provided on synthetic DNA (Integrated DNA Technologies). Each plasmid sequence was verified
385 by whole plasmid sequencing (Plasmidsaurus). Lentivirus was generated by co-transfection of
386 HEK293T cells with destination vector plasmid DNA and the packaging plasmids pMDLg/pRRE (Ad-
387 dgene, 12251), pRSV-Rev, (Addgene, 12253) and pMD2.G (Addgene, 12259) using FuGENE transfec-
388 tion reagent (Fisher, PRE2693) in DMEM (Fisher, MT10017CV) without FBS or penicillin-streptomycin.
389 The supernatant containing lentiviral particles was filtered through a 0.45 μ M membrane (Fisher,
390 9720514) and was supplemented with 8 μ g/ μ L polybrene (Sigma, TR-1003-G) prior to infection. For
391 infection, cells were seeded at 50% confluence in 6 well dishes and centrifuged with lentivirus (900g,
392 90 mins, 30°C). After 24 hours the media was replaced with fresh media and after 48 hours cells
393 were treated with either 1 μ g/mL blasticidin (Fisher, R21001) or 150 μ g/mL hygromycin (Sigma-
394 Aldrich, H7772-1G) and maintained in selection media until all uninfected control cells died. After
395 selection, cells were expanded and single-cell cloned by limiting dilution, plating 0.5 cells/well us-
396 ing 2-3 96 well plates. These clones were incubated until 10-30% confluence and screened for
397 high GFP and RFP signal using Incucyte S3 (Sartorius). The highest expressing monoclonal cells
398 were selected and further expanded on 6 well plates and again screened for fluorescence using
399 the Incucyte. From this a single clone was chosen, expanded and used for all subsequent experi-
400 ments. Different cell lines received different vector-sensor combinations: HEK293T cells were in-
401 fected with pLX304-CAG-jAspSnFR3-mRuby3 (blasticidin), HT1080 with pLenti-jAspSnFR3-mRuby3
402 (hygromycin) and HT1080, H1299 and H1299 GOT1/2 DKO cells expressing nuclear RFP were in-
403 fected with pLenti-jAspSnFR3 (hygromycin).

404 Generation of GOT1/2 double knockout (DKO) cells

405 Protocol and guide RNA generation was identical to that described in *Hart et al. (2023)*. Briefly,
406 three chemically synthesized 2'-O-methyl 3'phosphorothioate-modified single guide RNA (sgRNA)
407 sequences targeting GOT1 and GOT2 were purchased (Synthego; **Table 1**). A pool of all six sgRNAs
408 for GOT1 and GOT2 were resuspended in nuclease-free water, combined with SF buffer (Lonza,
409 V4XC-2032), and sNLS-spCas9 (Aldevron, 9212). 200,000 H1299 cells were resuspended in the re-
410 sulting solution containing ribonucleoprotein complexes (RNPs) and electroporated using a 4D-
411 Nucleofector (Amaxa, Lonza). Nucleofected cells were then expanded and single-cell cloned by
412 limiting dilution by plating 0.5 cells/well in a 96 well plate. Gene knockout was confirmed using
413 western blots.

Table 1. CRISPR guides.

Gene	sgRNA sequence (5'-3')
GOT1	CAGUCAUCCGUGCGAUAUGC GCACCGGAUGACUGGCCAUCCC CGAUCUUCUCCAUCUGGGAA
GOT2	UUUCUCAUUUCAGCUCCUGG CGGACGCUAGGCAGAACGUA UCCUUCCACUGUUCCGGACG

414 Intracellular jAspSnFR3 measurements

415 Experiments were conducted in DMEM without pyruvate (Corning 50-013-PB) supplemented with
416 3.7 g/L sodium bicarbonate 10% dialyzed fetal bovine serum (FBS) (Sigma-Aldrich, F0392) and 1%
417 penicillin-streptomycin solution. To start an experiment, cells were trypsinized (Corning, 25051CI),
418 resuspended in media, counted using a coulter counter (Beckman Coulter, Multisizer 4) and seeded
419 onto 24-well dishes (Nunc, 142475) with an initial seeding density of 50,000, 70,000, 70,000 or
420 150,000 cells/well for H1299, H1299 GOT1/2 DKO, HT1080 and HEK293T, respectively. After 24h
421 (H1299, HT1080, HEK293T) or 48h (H1299 GOT1/2 DKO) incubation, treatment was added and
422 plates moved into an Incucyte S3 (Sartorius) live cell imaging platform inside a humidified incubator
423 at 37°C with 5% CO₂. Rotenone (Sigma-Aldrich, R8875), metformin (Sigma-Aldrich, D150959), an-
424 timycin A (Sigma-Aldrich, A8674), oligomycin A (Sigma-Aldrich, 495455) and BAM15 (Cayman Chem-
425 ical, 17811) treatments were spiked-in as 20x solutions in water and the 2 mM pyruvate (Sigma-
426 Aldrich, P8574) was added as 500x stock in water. For treatments with varying media aspartate
427 (Sigma-Aldrich, A7219) or glutamine (Sigma-Aldrich, G5792), wells were washed thrice and filled
428 with media deplete of the given amino acid, then it was added as a spike-in at the specified concen-
429 tration from a 20x solutions in water. For plates receiving asparagine (Sigma-Aldrich, A7094), this
430 was added to 1 mM from a 20x solution in water, with vehicle wells receiving water. Live cell imaging
431 was performed on the Incucyte S3 using the GFP and RFP channels with default exposure times. Im-
432 ages were processed using the associated Incucyte software to subtract background, define areas
433 of cell confluence and GFP/RFP signal and extract the sum of the fluorescence signal in these areas.
434 The data for the GFP signal, RFP signal, GFP/RFP ratio and confluence for each well at each time-
435 point was exported and used for further data processing using Python code. The jAspSnFR3 signal
436 (GFP channel) was normalized to an RFP signal, either as a stably expressed nuclear localized RFP
437 (Nuc-RFP) or mRuby3 C-term fusion to jAspSnFR3. For some experiments the Nuc-RFP was used
438 to estimate cell counts per well by counting the number of nuclear foci in each field of view when
439 scanning in the RFP channel. Cell confluence was determined with the phase contrast scans using
440 the associated Incucyte software. For some experiments a pre-treatment scan was made shortly
441 prior to treatment to normalize the data to this point. For temporal measurements without a pre-
442 treatment scan, the first scan was made 30 min after treatment with subsequent scans indicated
443 on relevant plots. For comparisons of near steady-state measurements of GFP/RFP versus mass
444 spectrometry based metabolite measurements, a single scan was made 24 h after treatment, the
445 plate was then quickly moved to ice and metabolite extraction performed (see below). Another
446 plate was processed in parallel for cell volume determination using a coulter counter and aver-
447 aging across three replicate wells. The normalized jAspSnFR3 signal as a function of intracellular
448 aspartate concentration, $f(c)$, was fitted by a baseline shifted Hill curve:

$$f(c) = t + \frac{b - t}{1 + (c/m)^s}$$

449 With t , b being the top and bottom of the curve, respectively, describing the upper and lower
450 asymptotes of normalized jAspSnFR3 signal. The curve slope is described by s , also known as Hill co-
451 efficient, and the midpoint (m) describes the intracellular aspartate concentration at half maximum

452 jAspSnFR3 signal. The curve parameters were fitted to the data using the Broyden–Fletcher–Goldfarb–Shann
453 (BFGS) algorithm with an upper bound constraint on the top of the curve of 1.2 times the maximum
454 observed normalized jAspSnFR3 signal in any of the conditions on the same plot. Note that this
455 curve is not intended to represent a mechanistic model of the binding kinetics, rather the purpose
456 is to infer a reasonable estimate of the intracellular aspartate concentration at half maximum jAsp-
457 SnFR3 signal.

458 **Metabolite extraction**

459 For polar metabolite extraction, a plate was move to ice and the media was thoroughly aspirated.
460 For H1299 and HT1080 cells, wells were washed once with cold saline (Fisher, 23293184). For
461 HEK293T cells, washing was omitted due to weak cell adherence. Then, 1 mL 80% HPLC grade
462 methanol in HPLC grade water was added, cells were scraped with the back of a P1000 pipet tip
463 and transferred to Eppendorf tubes. Tubes were centrifuged (17,000g, 15 mins, 4°C) and 800 μ L of
464 the supernatant containing polar metabolites was transferred to a new centrifuge tube and placed
465 in a centrifrap until dry.

466 **Intracellular amino acid concentration measurements by isotope dilution**

467 Dried samples were reconstituted with 40 μ L 80% HPLC grade methanol containing 5 μ M U-13C,
468 U-15N labelled canonical amino acid mix (Cambridge Isotope Laboratories, MSK-CAA-1) and trans-
469 ferred to vials for measurement by LCMS. The peak area for each amino acid was divided by its la-
470 belled standard to derive the response ratio. The response ratio was then mapped to a calibration
471 curve to infer the amino acid concentration and finally the intracellular concentration was calcu-
472 lated by correcting for each step introducing a dilution, including the use of the total cell volume.
473 To make the calibration curves a non-labelled amino acid mixture was made from an analytical
474 amino acid standard without glutamine and asparagine (Sigma-Aldrich, A9906-1ML) and added
475 glutamine (Sigma-Aldrich, 76523-100MG) and asparagine (Sigma-Aldrich, 51363-100MG) to match
476 the concentration of the other amino acids. Using this mix, three replicates of a 12 point 2-fold
477 dilution series was made with a max concentration of 500 μ M and a volume per dilution of 40 μ L.
478 These were placed in a centrifrap until dry and reconstituted with 40 μ L 80% HPLC grade methanol
479 containing 5 μ M U-13C, U-15N labelled canonical amino acid mix (Cambridge Isotope Laboratories,
480 MSK-CAA-1) and transferred to vials for measurement by LCMS. The peak area for each amino acid
481 was divided by its labelled standard to derive the response ratio, then the best fitting calibration
482 curves for each amino acid were chosen among either linear, power or a second-degree polyno-
483 mial. Each calibration curve was manually inspected for proper fit and measurements below or
484 above the concentration range of the dilution series were discarded.

485 **Liquid Chromatography-Mass Spectrometry (LCMS)**

486 Metabolite quantitation was performed using a Q Exactive HF-X Hybrid Quadrupole-Orbitrap Mass
487 Spectrometer equipped with an Ion Max API source and H-ESI II probe, coupled to a Vanquish Flex
488 Binary UHPLC system (Thermo Scientific). Mass calibrations were completed at a minimum of ev-
489 ery 5 days in both the positive and negative polarity modes using LTQ Velos ESI Calibration Solution
490 (Pierce). Polar Samples were chromatographically separated by injecting a sample volume of 1 μ L
491 into a SeQuant ZIC-pHILIC Polymeric column (2.1 x 150 mm 5 mM, EMD Millipore). The flow rate
492 was set to 150 mL/min, autosampler temperature set to 10 °C, and column temperature set to 30°C.
493 Mobile Phase A consisted of 20 mM ammonium carbonate and 0.1% (v/v) ammonium hydroxide,
494 and Mobile Phase B consisted of 100% acetonitrile. The sample was gradient eluted (%B) from the
495 column as follows: 0-20 min.: linear gradient from 85% to 20% B; 20-24 min.: hold at 20% B; 24-
496 24.5 min.: linear gradient from 20% to 85% B; 24.5 min.-end: hold at 85% B until equilibrated with
497 ten column volumes. Mobile Phase was directed into the ion source with the following parameters:
498 sheath gas = 45, auxiliary gas = 15, sweep gas = 2, spray voltage = 2.9 kV in the negative mode or 3.5

499 kV in the positive mode, capillary temperature = 300°C, RF level = 40%, auxiliary gas heater temper-
500 ature = 325°C. Mass detection was conducted with a resolution of 240,000 in full scan mode, with
501 an AGC target of 3,000,000 and maximum injection time of 250 msec. Metabolites were detected
502 over a mass range of 70-850 m/z. Quantitation of all metabolites was performed using Tracefinder
503 4.1 (Thermo Scientific) referencing an in-house metabolite standards library using ≤ 5 ppm mass
504 error.

505 **Data analysis and plotting**

506 All data processing, curve fitting, plotting and statistics for experiments involving jAspSnFR3 ex-
507 pressed in cell lines was made using Python code and data available on Github: www.github.com/krdav/Aspartate-sensor

509 **Plasmid availability**

510 Submitted to Addgene under article ID 28238106.

511 **Acknowledgement**

512 We would like to acknowledge Kaspar Podgorski for pre-publication plasmid access to iGluSnFR3
513 variants and Ronak Patel for the 2P spectral analysis.

514 **Funding**

515 This research was supported by the Proteomics & Metabolomics Shared Resource of the Fred
516 Hutch/University of Washington/Seattle Children's Cancer Consortium (P30 CA015704). L.B.S. ac-
517 knowledges support from the National Institute of General Medical Sciences (NIGMS; R35GM147118).
518 J.S.M. and T.A.B. are funded by the Howard Hughes Medical Institute.

519 **References**

520 Aggarwal A, Liu R, Chen Y, Ralowicz AJ, Bergerson SJ, Tomaska F, Mohar B, Hanson TL, Hasseman JP, Reep D,
521 Tsegaye G, Yao P, Ji X, Kloos M, Walpita D, Patel R, Mohr MA, Tillberg PW, GENIE Project Team, Looger LL, et al.
522 Glutamate indicators with improved activation kinetics and localization for imaging synaptic transmission.
523 Nat Methods. 2023 May; 20(5):925-934.

524 Andrzejewski S, Gravel SP, Pollak M, St-Pierre J. Metformin directly acts on mitochondria to alter cellular
525 bioenergetics. Cancer Metab. 2014 Aug; 2:12.

526 Arnold PK, Jackson BT, Paras KI, Brunner JS, Hart ML, Newsom OJ, Alibekoff SP, Endress J, Drill E, Sullivan LB,
527 Finley LWS. A non-canonical tricarboxylic acid cycle underlies cellular identity. Nature. 2022 Mar; p. 1-5.

528 Bailis W, Shyer JA, Zhao J, Canaveras JCG, Al Khazal FJ, Qu R, Steach HR, Bielecki P, Khan O, Jackson R, Kluger Y,
529 Maher LJ 3rd, Rabinowitz J, Craft J, Flavell RA. Distinct modes of mitochondrial metabolism uncouple T cell
530 differentiation and function. Nature. 2019 Jul; 571(7765):403-407.

531 Birsoy K, Wang T, Chen WW, Freinkman E, Abu-Remaileh M, Sabatini DM. An Essential Role of the Mitochondrial
532 Electron Transport Chain in Cell Proliferation Is to Enable Aspartate Synthesis. Cell. 2015 Jul; 162(3):540-551.

533 Brand MD, Nicholls DG. Assessing mitochondrial dysfunction in cells. Biochem J. 2011 Apr; 435(2):297-312.

534 Cardaci S, Zheng L, MacKay G, van den Broek NJF, MacKenzie ED, Nixon C, Stevenson D, Tumanov S, Bulusu
535 V, Kamphorst JJ, Vazquez A, Fleming S, Schiavi F, Kalna G, Blyth K, Strathdee D, Gottlieb E. Pyruvate carboxy-
536 lation enables growth of SDH-deficient cells by supporting aspartate biosynthesis. Nat Cell Biol. 2015 Oct;
537 17(10):1317-1326.

538 Chen WW, Freinkman E, Wang T, Birsoy K, Sabatini DM. Absolute Quantification of Matrix Metabolites Reveals
539 the Dynamics of Mitochondrial Metabolism. Cell. 2016 Aug; 166(5):1324-1337.e11.

540 Diebold LP, Gil HJ, Gao P, Martinez CA, Weinberg SE, Chandel NS. Mitochondrial complex III is necessary for
541 endothelial cell proliferation during angiogenesis. Nat Metab. 2019 Jan; 1(1):158-171.

542 **Ei-Mir MY**, Nogueira V, Fontaine E, Averet N, Rigoulet M, Leverve X. Dimethylbiguanide Inhibits Cell Respiration
543 via an Indirect Effect Targeted on the Respiratory Chain Complex I *. *J Biol Chem.* 2000 Jan; 275(1):223–228.

544 **Garcia-Bermudez J**, Badgley MA, Prasad S, Baudrier L, Liu Y, La K, Soula M, Williams RT, Yamaguchi N, Hwang
545 RF, Taylor LJ, de Stanchina E, Rostandy B, Alwaseem H, Molina H, Bar-Sagi D, Birsoy K. Adaptive stimulation
546 of macropinocytosis overcomes aspartate limitation in cancer cells under hypoxia. *Nat Metab.* 2022 Jun;
547 4(6):724–738.

548 **Garcia-Bermudez J**, Baudrier L, La K, Zhu XG, Fidelin J, Sviderskiy VO, Papagiannakopoulos T, Molina H, Snuderl
549 M, Lewis CA, Possemato RL, Birsoy K. Aspartate is a limiting metabolite for cancer cell proliferation under
550 hypoxia and in tumours. *Nat Cell Biol.* 2018 Jul; 20(7):775–781.

551 **Gui DY**, Sullivan LB, Luengo A, Hosios AM, Bush LN, Gitego N, Davidson SM, Freinkman E, Thomas CJ, Vander Hei-
552 den MG. Environment Dictates Dependence on Mitochondrial Complex I for NAD⁺ and Aspartate Production
553 and Determines Cancer Cell Sensitivity to Metformin. *Cell Metab.* 2016 Nov; 24(5):716–727.

554 **Hart ML**, Quon E, Vigil ALBG, Engstrom IA, Newsom OJ, Davidsen K, Hoellerbauer P, Carlisle SM, Sullivan LB.
555 Mitochondrial redox adaptations enable alternative aspartate synthesis in SDH-deficient cells. *Elife.* 2023
556 Mar; 12.

557 **Helassa N**, Dürst CD, Coates C, Kerruth S, Arif U, Schulze C, Wiegert JS, Geeves M, Oertner TG, Török K. Ultrafast
558 glutamate sensors resolve high-frequency release at Schaffer collateral synapses. *Proc Natl Acad Sci U S A.*
559 2018 May; 115(21):5594–5599.

560 **Helenius IT**, Madala HR, Yeh JRJ. An Asp to Strike Out Cancer? Therapeutic Possibilities Arising from Aspartate's
561 Emerging Roles in Cell Proliferation and Survival. *Biomolecules.* 2021 Nov; 11(11).

562 **Hellweg L**, Pfeifer M, Chang L, Tarnawski M, Bergner A, Kress J, Hiblot J, Reinhardt J, Johnsson K, Leippe P.
563 Engineering of a biosensor for intracellular aspartate. *bioRxiv.* 2023; <https://www.biorxiv.org/content/early/2023/05/04/2023.05.04.537313>, doi: [10.1101/2023.05.04.537313](https://doi.org/10.1101/2023.05.04.537313).

565 **Hu Y**, Fan CP, Fu G, Zhu D, Jin Q, Wang DC. Crystal structure of a glutamate/aspartate binding protein complexed
566 with a glutamate molecule: structural basis of ligand specificity at atomic resolution. *J Mol Biol.* 2008 Sep;
567 382(1):99–111.

568 **Jarmoskaite I**, AlSadhan I, Vaidyanathan PP, Herschlag D. How to measure and evaluate binding affinities. *Elife.*
569 2020 Aug; 9.

570 **Kenwood BM**, Weaver JL, Bajwa A, Poon IK, Byrne FL, Murrow BA, Calderone JA, Huang L, Divakaruni AS, Tomsig
571 JL, Okabe K, Lo RH, Cameron Coleman G, Columbus L, Yan Z, Saucerman JJ, Smith JS, Holmes JW, Lynch KR,
572 Ravichandran KS, et al. Identification of a novel mitochondrial uncoupler that does not depolarize the plasma
573 membrane. *Mol Metab.* 2014 Apr; 3(2):114–123.

574 **Kostyuk AI**, Demidovich AD, Kotova DA, Belousov VV, Bilan DS. Circularly Permuted Fluorescent Protein-Based
575 Indicators: History, Principles, and Classification. *Int J Mol Sci.* 2019 Aug; 20(17).

576 **Koveal D**, Díaz-García CM, Yellen G. Fluorescent Biosensors for Neuronal Metabolism and the Challenges of
577 Quantitation. *Curr Opin Neurobiol.* 2020 Aug; 63:111–121.

578 **Kunkel TA**. Rapid and efficient site-specific mutagenesis without phenotypic selection. *Proc Natl Acad Sci U S*
579 *A.* 1985 Jan; 82(2):488–492.

580 **Marvin JS**, Borghuis BG, Tian L, Cichon J, Harnett MT, Akerboom J, Gordus A, Renninger SL, Chen TW, Bargmann
581 CI, Orger MB, Schreiter ER, Demb JB, Gan WB, Hires SA, Looger LL. An optimized fluorescent probe for
582 visualizing glutamate neurotransmission. *Nat Methods.* 2013 Feb; 10(2):162–170.

583 **Marvin JS**, Scholl B, Wilson DE, Podgorski K, Kazemipour A, Müller JA, Schoch S, Quiroz FJU, Rebola N, Bao
584 H, Little JP, Tkachuk AN, Cai E, Hantman AW, Wang SSH, DePiero VJ, Borghuis BG, Chapman ER, Dietrich D,
585 DiGregorio DA, et al. Stability, affinity, and chromatic variants of the glutamate sensor iGluSnFR. *Nat Methods.*
586 2018 Nov; 15(11):936–939.

587 **Owen MR**, Doran E, Halestrap AP. Evidence that metformin exerts its anti-diabetic effects through inhibition
588 of complex 1 of the mitochondrial respiratory chain. *Biochem J.* 2000 Jun; 348 Pt 3:607–614.

589 **Park JO**, Rubin SA, Xu YF, Amador-Noguez D, Fan J, Shlomi T, Rabinowitz JD. Metabolite concentrations, fluxes
590 and free energies imply efficient enzyme usage. *Nat Chem Biol.* 2016 Jul; 12(7):482–489.

591 **Patel D**, Menon D, Bernfeld E, Mroz V, Kalan S, Loayza D, Foster DA. Aspartate Rescues S-phase Arrest Caused by
592 Suppression of Glutamine Utilization in KRas-driven Cancer Cells. *J Biol Chem.* 2016 Apr; 291(17):9322–9329.

593 **Pavlova NN**, Hui S, Ghergurovich JM, Fan J, Intlekofer AM, White RM, Rabinowitz JD, Thompson CB, Zhang J. As
594 Extracellular Glutamine Levels Decline, Asparagine Becomes an Essential Amino Acid. *Cell Metab.* 2018 Feb;
595 27(2):428–438.e5.

596 **Qi L**, Martin-Sandoval MS, Merchant S, Gu W, Eckhardt M, Mathews TP, Zhao Z, Agathocleous M, Morrison SJ.
597 Aspartate availability limits hematopoietic stem cell function during hematopoietic regeneration. *Cell Stem Cell.* 2021 Aug; .

599 **Studier FW**. Protein production by auto-induction in high density shaking cultures. *Protein Expr Purif.* 2005
600 May; 41(1):207–234.

601 **Sullivan LB**, Gui DY, Hosios AM, Bush LN, Freinkman E, Vander Heiden MG. Supporting Aspartate Biosynthesis
602 Is an Essential Function of Respiration in Proliferating Cells. *Cell.* 2015 Jul; 162(3):552–563.

603 **Sullivan LB**, Luengo A, Danai LV, Bush LN, Diehl FF, Hosios AM, Lau AN, Elmiligy S, Malstrom S, Lewis CA, Van-
604 der Heiden MG. Aspartate is an endogenous metabolic limitation for tumour growth. *Nat Cell Biol.* 2018 Jul;
605 20(7):782–788.

606 **Symersky J**, Osowski D, Walters DE, Mueller DM. Oligomycin frames a common drug-binding site in the ATP
607 synthase. *Proc Natl Acad Sci U S A.* 2012 Aug; 109(35):13961–13965.

608 **To TL**, Cuadros AM, Shah H, Hung WHW, Li Y, Kim SH, Rubin DHF, Boe RH, Rath S, Eaton JK, Piccioni F, Goodale
609 A, Kalani Z, Doench JG, Root DE, Schreiber SL, Vafai SB, Mootha VK. A Compendium of Genetic Modifiers of
610 Mitochondrial Dysfunction Reveals Intra-organelle Buffering. *Cell.* 2019 Nov; 179(5):1222–1238.e17.

611 **Tournaire G**, Loopmans S, Stegen S, Rinaldi G, Eelen G, Torrekens S, Moermans K, Carmeliet P, Ghesquière
612 B, Thienpont B, Fendt SM, van Gastel N, Carmeliet G. Skeletal progenitors preserve proliferation and
613 self-renewal upon inhibition of mitochondrial respiration by rerouting the TCA cycle. *Cell Rep.* 2022 Jul;
614 40(4):111105.

615 **Wheaton WW**, Weinberg SE, Hamanaka RB, Soberanes S, Sullivan LB, Anso E, Glasauer A, Dufour E, Mutlu GM,
616 Budigner GS, Chandel NS. Metformin inhibits mitochondrial complex I of cancer cells to reduce tumorigen-
617 esis. *Elife.* 2014 May; 3:e02242.

618 **Zhang J**, Fan J, Venneti S, Cross JR, Takagi T, Bhinder B, Djaballah H, Kanai M, Cheng EH, Judkins AR, Pawel B,
619 Baggs J, Cherry S, Rabinowitz JD, Thompson CB. Asparagine plays a critical role in regulating cellular adapta-
620 tion to glutamine depletion. *Mol Cell.* 2014 Oct; 56(2):205–218.

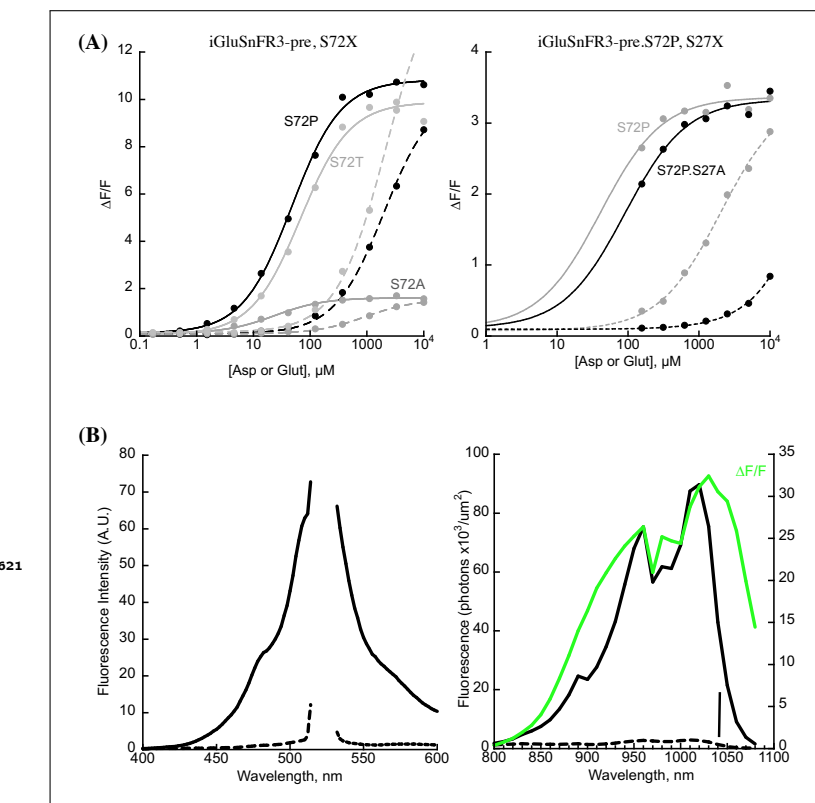


Figure 1—figure supplement 1. (A) Switching specificity of the iGluSnFR3 precursor from glutamate to aspartate using S72X library (left) and S72P, S27X library (right). Titrations with aspartate (solid lines) and glutamate (dashed lines) in bacterial lysate. (B) Excitation and emission spectra of jAspSnFR3-mRuby3. Left, 1-photon spectra. Excitation wavelength was varied from 400 nm to 520 nm (7.5 nm bandpass) while observing emission at 535 nm (10 nm bandpass). Emission wavelength was varied from 535 nm to 600 nm (10 nm bandpass) while exciting at 510 nm (7.5 nm bandpass). Fluorescence was measured both in the absence (dashed lines) and presence of 10 mM aspartate (solid lines). Right, 2-photon cross-sections, also ± 10 mM aspartate, with an overlay of calculated $\Delta F/F$ (green). Vertical bar indicates 1040 nm.

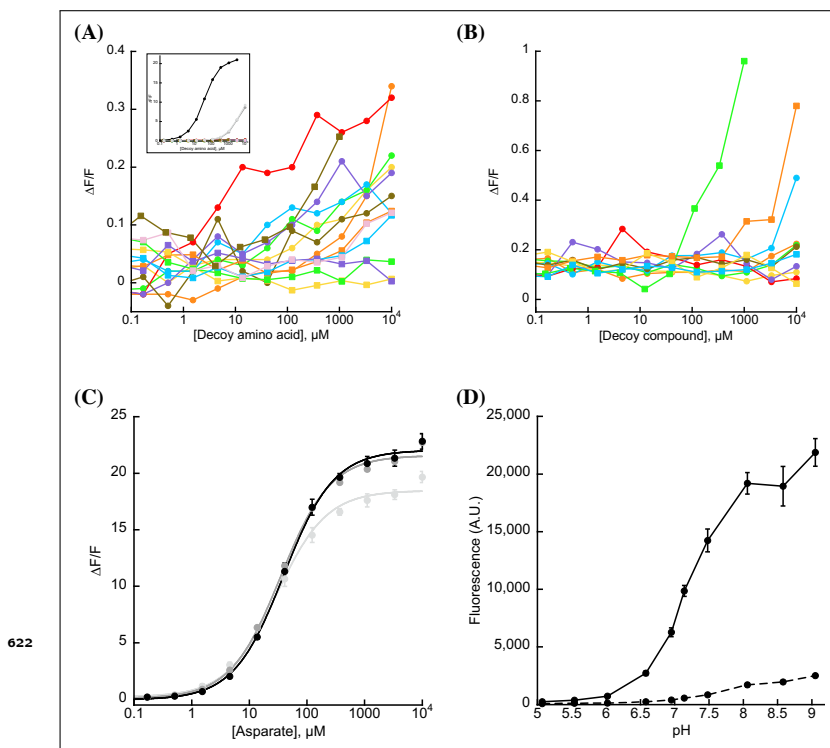
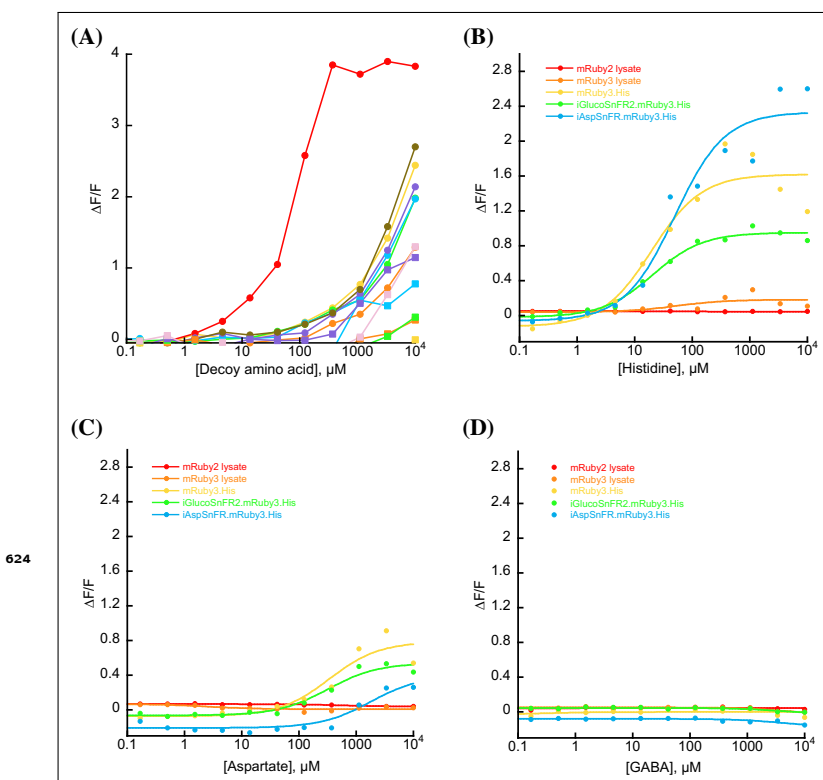
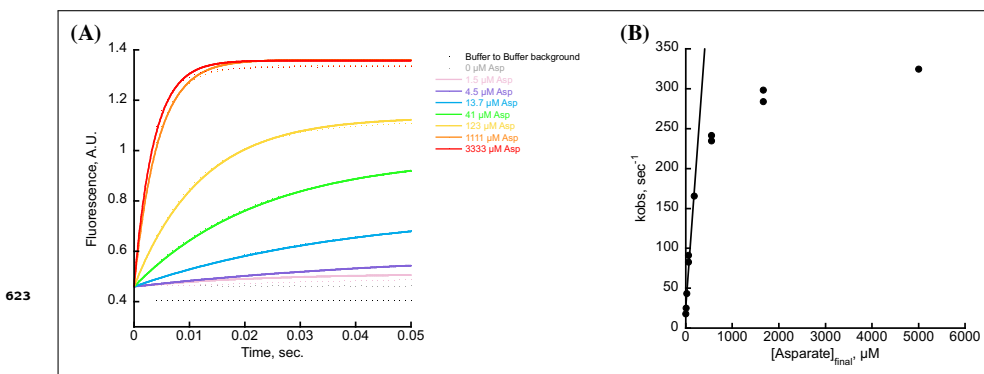


Figure 1—figure supplement 2. (A) jAspSnFR3-mRuby3 does not appreciably change its green fluorescence in response to other amino acids (alanine, phenylalanine, glycine, histidine (red line), isoleucine, leucine, methionine, proline, glutamine, arginine, serine, threonine, valine, or tryptophan). Insert with aspartate in black and glutamate/asparagine in grey for comparison. Ex. 485 nm (20 nm bandpass), Em. 535 nm (20 nm bandpass), 0.2 μM purified protein in PBS. (B) jAspSnFR3-mRuby3 does not respond to other decoys: citrate, lactate, pyruvate, malate, alpha-ketoglutarate, cis-aconitate, succinate, fumarate, or oxaloacetate (orange squares); nor to relevant pharmacological treatments: rotenone (green squares) or metformin. The small increase in fluorescence from rotenone is likely due to the scattering of a visibly turbid solution; rotenone has very low solubility in water. Ex. 485 nm (20 nm bandpass), Em. 535 nm (20 nm bandpass). (C) jAspSnFR3-mRuby3 is not adversely affected by temperature. Fluorescence as a function of aspartate titration at 23°C (light grey), 30°C (medium grey), and 37°C (black). Error bars are standard deviation of three technical replicates. (D) pH sensitivity of jAspSnFR3-mRuby3 (green component). Ex 485 nm (5 nm bp), Em 515 nm (10 nm bp). Error bars are standard deviation of 5 technical replicates. Solid line is with 3 mM aspartate, dashed line is without aspartate.



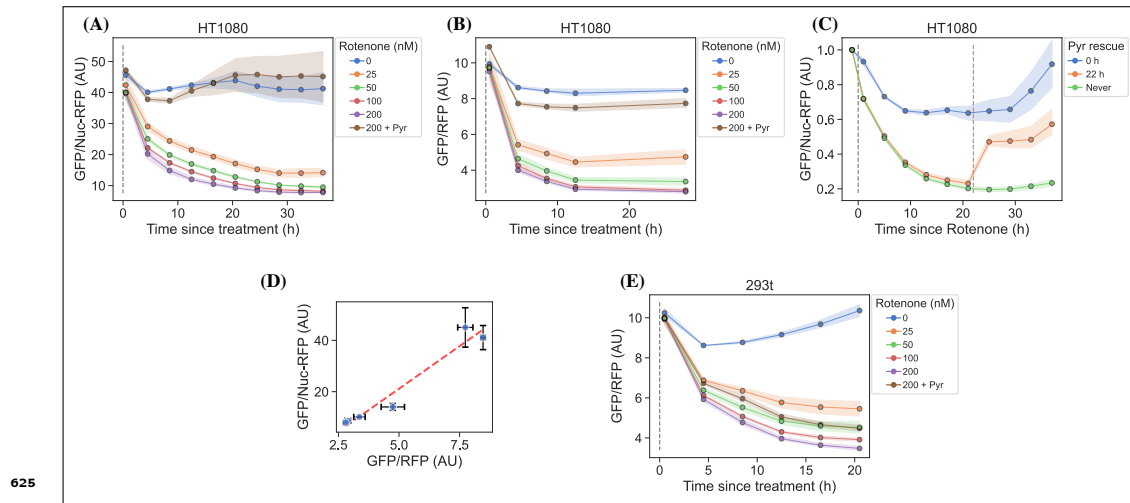


Figure 2—figure supplement 1. jAspSnFR3 temporal response after rotenone treatment. (A) HT1080 cells using nuclear RFP to normalize the jAspSnFR3 signal, treated with a rotenone titration. (B) HT1080 cells using an RFP fused to jAspSnFR3 (jAspSnFR3-mRuby3) for normalization, treated with a rotenone titration. (C) HT1080 cells treated with 100 nM rotenone at the start of the experiment (0 h) and then rescued with pyruvate at start, 22 h or never. (D) Comparison between the steady-state signal of (A) and (B) with a linear regression shown as a red dashed line to show that nuclear RFP and RFP fusion normalizations are equivalent. (E) HEK293t cells using an RFP fused to jAspSnFR3 for normalization, treated with a rotenone titration. For plots (A), (B), (C) and (E) markers indicate the average using available well replicates and are superimposed on a bootstrapped 95% confidence interval colored using the same color code as the markers. For plot (D) markers indicate the average using available well replicates and errorbars are drawn as +/- the standard deviation of the replicates. Grey dashed lines indicate the time of treatment. Orange dashed line in panel (C) indicates time of pyruvate addition. AU, arbitrary unit.

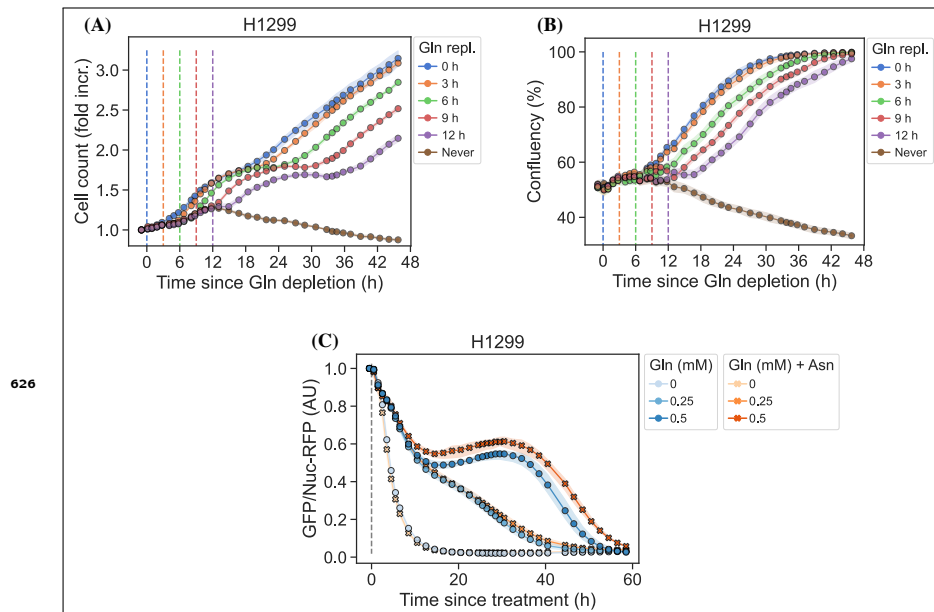


Figure 2—figure supplement 2. (A) Nuclei count over time for conditions displayed in Figure 2, panel E. (B) Cell confluency over time for conditions displayed in Figure 2, panel E. (C) H1299 cells changed into media with a titration of glutamine with or without 1 mM asparagine. Identical to Figure 2, panel H but with fewer glutamine concentrations and more well replicates.

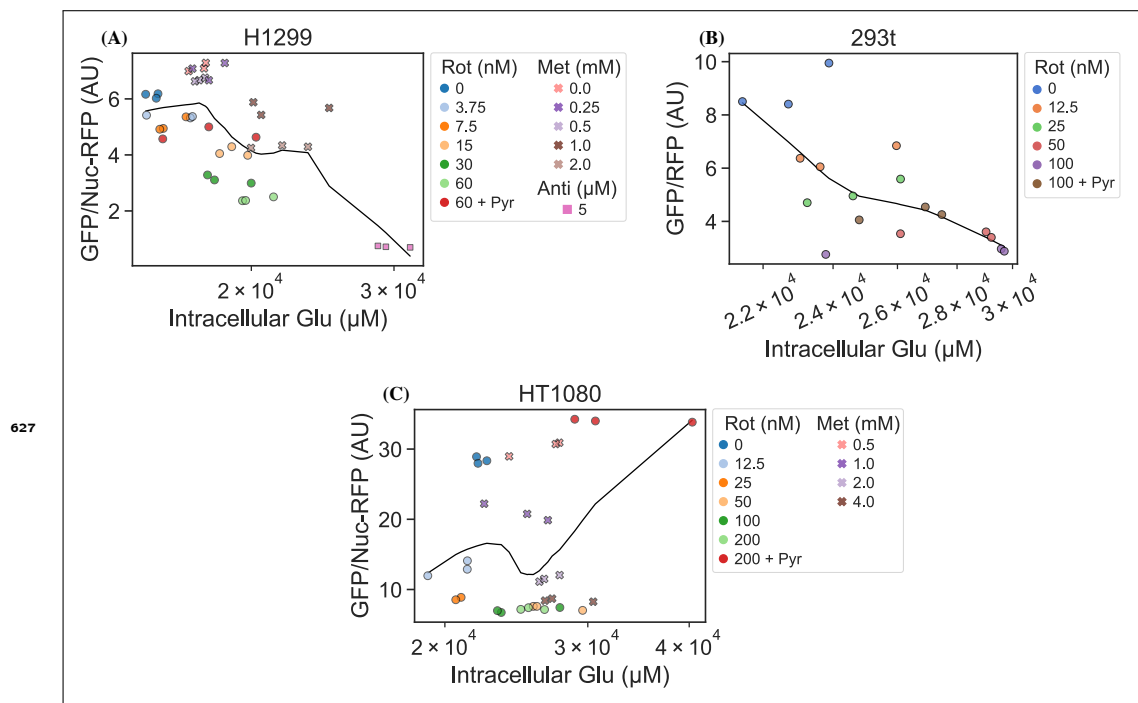


Figure 3—figure supplement 1. RFP normalized jAspSnFR3 signal, following various perturbations to live cells, is not correlated with the LCMS measured intracellular glutamate concentration. Datapoints are fitted to a local linear regression, shown by the black line, otherwise, these plots are identical to those in **Figure 3**. AU, arbitrary unit.